Supplementary Materials

A cluster-type self-healing catalyst for stable saline-alkali water splitting

Haiming Wang[1,2] and Sheng Chen[1,*]

[1] Key Laboratory for Soft Chemistry and Functional Materials (Ministry of Education), School of Chemical Engineering, Nanjing University of Science and Technology, Nanjing, Jiangsu 210094, China

[2] College of Mechanical and Electronic Engineering, Tarim University, Alaer, Xinjiang 843300, China

* Corresponding e-mail: sheng.chen@njust.edu.cn

1. Chemicals.

2-hiophenecarboxylic acid (2-$C_5H_4O_2S$, 99%) was purchased from Tianjing Heowns Biochemical Technology Co., Ltd. Nickel acetate tetrahydrate ($Ni(Ac)_2 \cdot 4H_2O$,99%), ferric(III) nitrate nonahydrate ($Fe(NO_3)_3 \cdot 9H_2O$, 98.5%), and potassium hydroxide (KOH, 95%) were obtained from Shanghai Macklin Biochemical Technology Co., Ltd. High purity potassium hydroxide (KOH, electronic grade, 99.999%) was purchased from Shanghai Aladdin Biochemical Technology Co., LTD. Ethanol (absolute alcohol, AR) was purchased from Sinopharm Chemical Reagent Co., Ltd. IrO_2 were obtained from Afar Aesa. All chemicals were used as they were received from manufacturers. All aqueous solution was prepared with high-purity de-ionized water (DI-water, resistance 18.25 MΩ cm^{-1}). Nickel foam (NF, 2.8 cm×2 cm×1.6 mm, surface density 380 g m^{-2}, PPI 110, porosity > 95%, purity 99.8%) Iron foam (IF, 2.8 cm×2 cm×1.6 mm, surface density 1420 g m^{-2}, PPI 95, porosity > 95%, purity 99.8%), Nickel Iron foam (NIF, 2.8 cm×2 cm×1.6 mm, PPI 95, porosity > 95%, purity 99.8%, surface density 1130 g m^{-2} ($Ni_{0.5}Fe_{0.5}$, 50 wt% Fe), were purchased from Suzhou Sinero Technology Co., Ltd. Nickel foam was washed successively with dilute HCl solution, absolute alcohol and DI-water under ultrasonication for 5 min, respectively, which was used to remove the surface oxide layer and organic residue. Then the clean nickel foam was immersed in absolute alcohol for use.

2. Characterizations

Scanning electron microscopy was conducted on a field emission scanning electron microscope (FESEM, JEOL 7800F). Transmission electron microscope (TEM) and high-resolution transmission electron microscope (HRTEM) were conducted on an aberration-corrected TEM (Thermo Scientific-Talos^{TM} F200i, 200 kV acceleration Voltage). Energy-dispersive X-ray spectroscopy (EDS) and element mapping were acquired on SEM (OXFORD X-Max^{N} 150 10 kV). X-ray diffractions were conducted on X-ray diffractometer (XRD, Bruker-AXS D8 Advance 3 kW, 40 kV, 40 mA, λ=1.5418 Å) with Cu-Kα radiation. X-ray photoelectron spectroscopy (XPS) was collected between 4 and 200 eV on an Axis Ultra (ThermoScientific^{TM} K-Alpha) XPS spectrometer equipped with an Al Kα source (1486.6 eV). FTIR spectra were recorded in a Thermofisher NICOLETIS 20 FTIR spectrometer. Inductively coupled plasma mass spectroscopy (ICP-MS) measurements were carried on Agilent 7800. Ion Chromatography (IC,Thermo Scientific ICS-600) was used to the anion content of saline-alkali water. Atomic Force Microscopy (AFM) was conducted on Bruker Dimension ICON SPM using peak force mode. UV-vis spectra were collected on a SHIMADZU UV-2600 spectrophotometer. Raman measurements were performed using a Renishaw inVia Raman Scope system with 532 nm wavelength incident laser light and 100 mW power.

3. Electrochemical measurements

Electrochemical tests were performed on a CHI 760E electrochemical workstation. Specifically, OER was tested in a three-electrode system in a single electrolytic cell with 1-6 M Nickel clusters (NC)/KOH+ saline-alkali water (SAW) mixed solution (with 85% *iR*-compensation), which used Ni_xFe_yOOH, graphite rod and Hg/HgO (1 M KOH) as working, counter and reference electrodes, respectively.

The OER overpotential vs. $E_{Hg/HgO}$ measured in this study can be converted to corresponding overpotentials using the following equation:

$$\eta = E_{Hg/HgO} + 0.059 \times pH + 0.098 - 1.23\ V$$

Linear sweep voltammogram plots (LSVs) were recorded at a scan rate of 5 mV s^{-1} from 2.1 to 0.9 V (vs. RHE, reverse scans). All LSV plots were recorded with 85% *iR*-compensation. The Tafel slope was calculated according to Tafel equation as follows:

$$\eta = b\log j + a$$

where η is overpotential (V), j is current density (mA cm^{-2}), and b is Tafel slope (mV dec^{-1}).

The long-term durability was tested by chronopotentiometry at 100 mA or 500 mA for OER up to 100 h without iR-compensation. The corresponding LSVs before and after electrochemical testing were collected with 85% iR-compensation for comparison purpose. In addition, electric double layer capacitances (C_{dl}, mF cm^{-2}) of working electrodes were obtained from double-layer charge-discharge diagram using cyclic voltammetry (CV) in a small potential range of 1.12~1.22 V (vs. RHE). Both a plot of the $\Delta J = (J_a - J_c)/2$(mA) at 1.17 V (vs.RHE) against scan rate are nearly linear and the double layer capacitance were obtained by its slopes. Based on the reported method, we have used a benchmark capacitance of C_s= 0.04 mF cm^{-2} (typical reported value) to calculate electrochemically active surface area (ECSA, denoted as A_{ECSA}) of

various electrodes ($A_{ECSA} = C_{dl}/C_s$ (per cm^{-2})) [1]. The use of geometric area (GA, denoted as A_{GA}) for current normalization (denoted as J_{GA}) could be traced back to the period when smooth planar electrodes were widely used in the electrochemical community, and it could be calculated based on the dimension of the surface contacting the electrolyte: $A_{GA} = 2hl + wl + 2wh$ [2]. In most cases, the thickness of the planar electrode is much smaller than its length and height, thus $A_{GA} \approx 2hl$, A_{GA} is 1 cm^2 in this work (A_{GA} = 2 x 0.5 cm x 1 cm=1 cm^2). Electrochemical impedance spectroscopy (EIS) was measured at 1.197 V (vs. Hg/HgO) from 100 KHz to 0.01 Hz. Faraday efficiency (FE) for OER was measured in a H-type electrolytic cell with Ni_xFe_yOOH, graphite rod and Hg/HgO (1 M KOH) as anode, cathode and reference electrodes, respectively. FE was calculated based on the equation: $FE = V_{exp.} / V_{the.} = V_{exp.} / (V_m Q / (n F)) = V_{exp.} / (V_m i t / (n F))$, where $V_{exp.}$ is the experimental volume of O_2, $V_{the.}$ is the theoretical volume of O_2, V_m is the molar volume of gas (25°C,24.5 L mol^{-1}), Q is the amount of electric charge, n is the number of electrons transferred; F is faraday constant (96,485 C mol^{-1}); i is the test current, t is the collection time of O_2 [3].

Overall water splitting was conducted in a two-electrode system by employing Ni_xFe_yOOH || Pt/C electrodes as anode and cathode, respectively. The long-term durability was tested by chronopotentiometry at 500 mA cm^{-2} for Overall water splitting up to 100 h without iR-compensation.

4. Supplementary Results

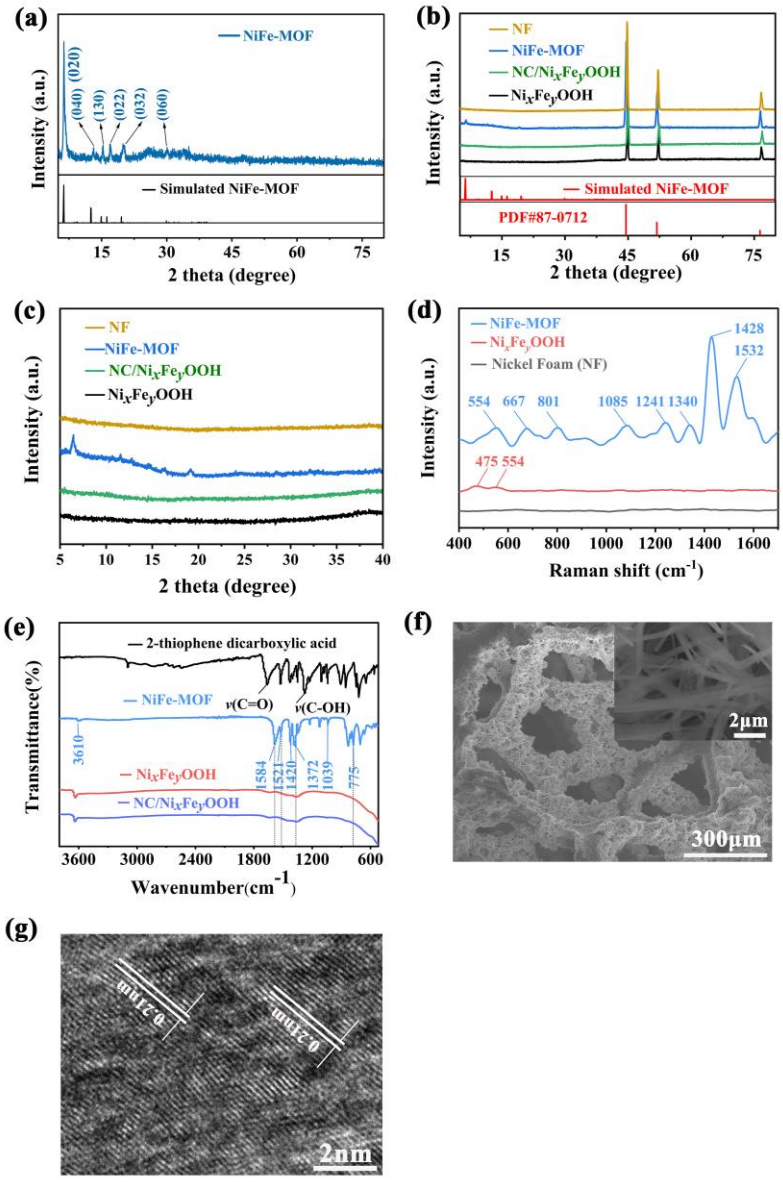

Figure S1. XRD patterns of NiFe-MOF and reconstructions.

(a) NiFe-MOF, (b) NiFe-MOF and reconstructions, (c) partially amplified spectrum, (d) Raman spectra of NF, NiFe-MOF, and Ni_xFe_yOOH, (e) FTIR spectra of thiophene, NiFe-MOF, and NixFeyOOH, (f) SEM images of Ni_xFe_yOOH, the inset of (f) is nanoribbon structure; (g) HRTEM image of Ni_xFe_yOOH.

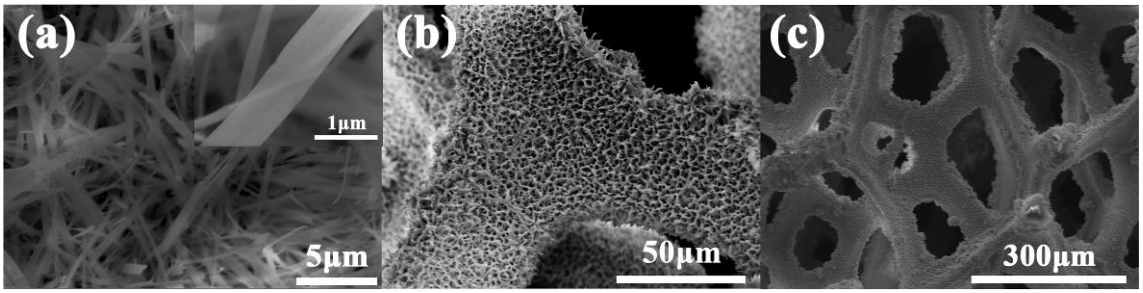

Figure S2. Morphology characterizations of NiFe-MOF.

(a-c) SEM images, inset of (a) is a nanoribbon.

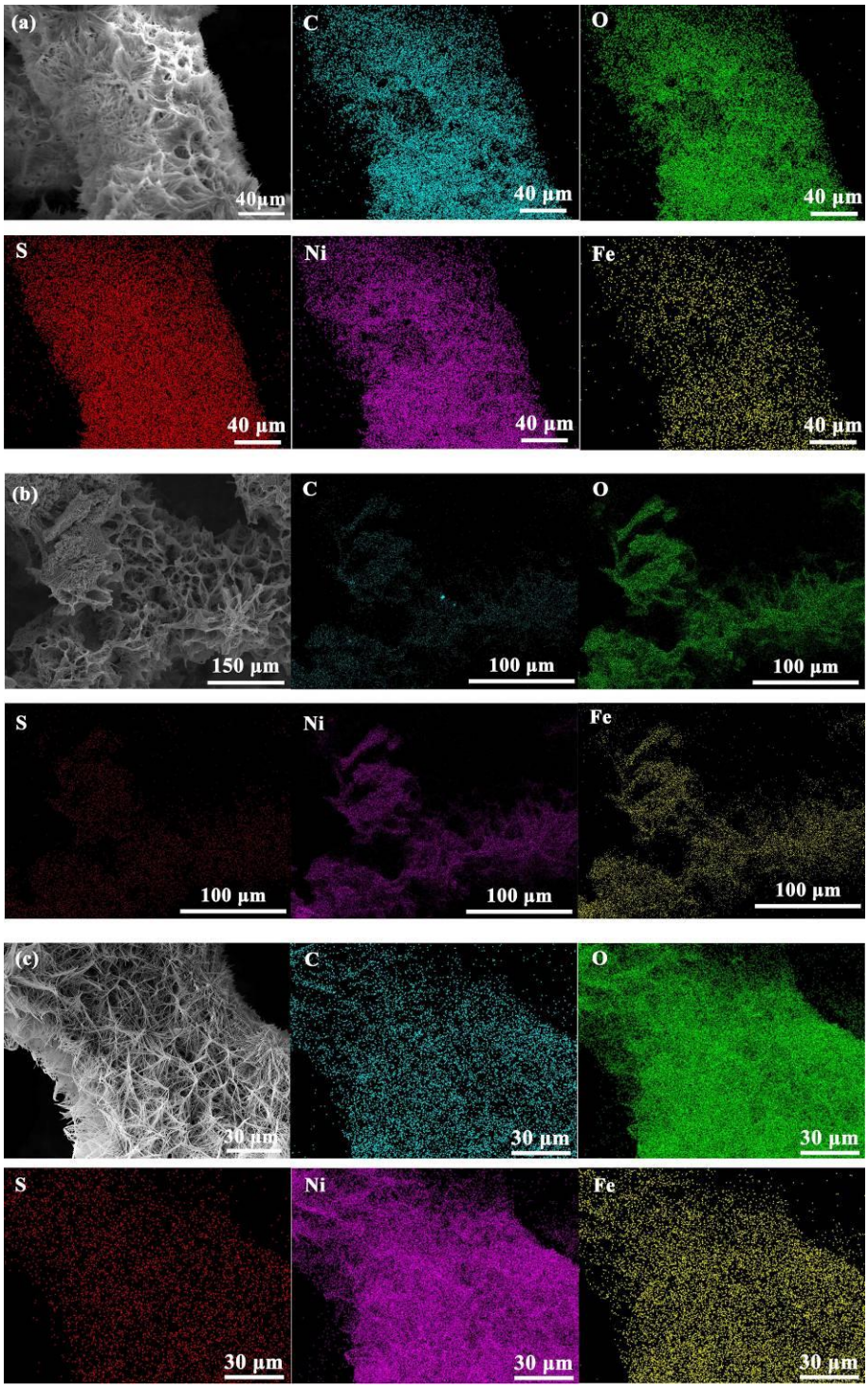

Figure S3. SEM Mappings of different electrocatalysts.

(a) NiFe-MOF, (b) Ni_xFe_yOOH, (c) NC/Ni_xFe_yOOH.

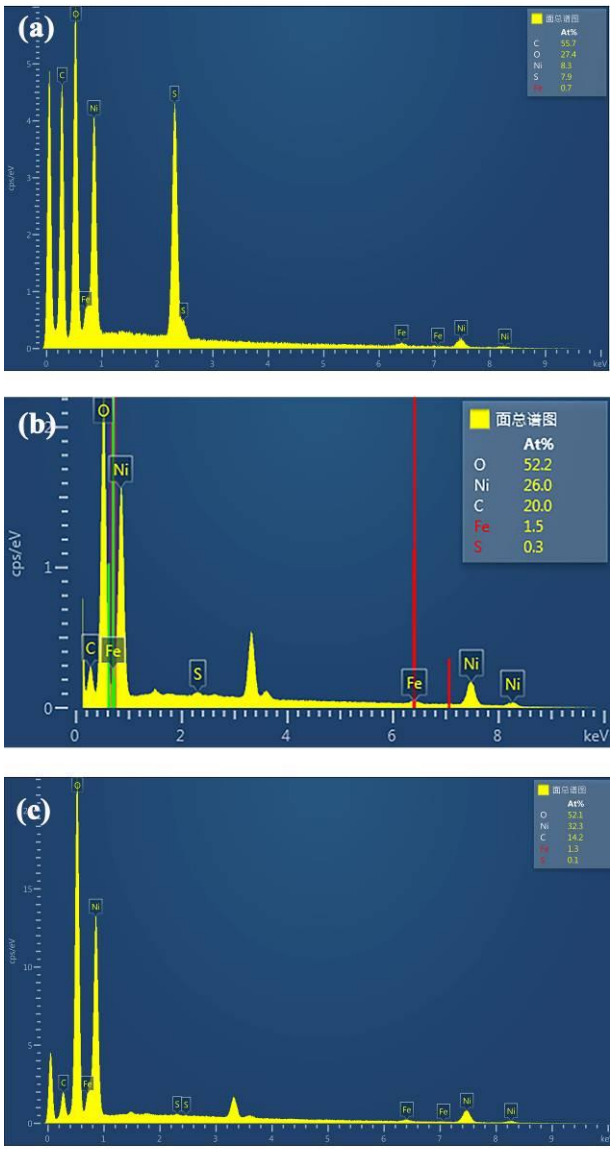

Figure S4. SEM EDS of different electrocatalysts.

(a) NiFe-MOF, (b) Ni_xFe_yOOH, (c) NC/Ni_xFe_yOOH.

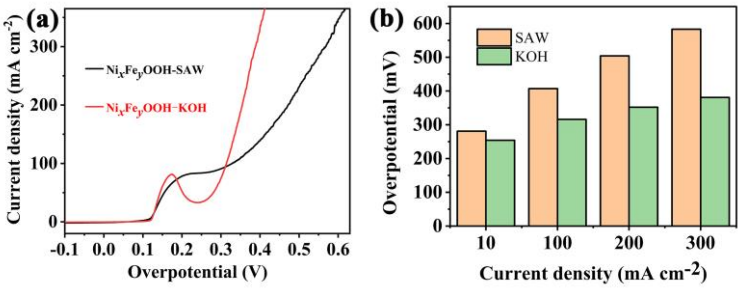

Figure S5.The activities of Ni_xFe_yOOH in KOH and saline-alkali water (SAW), respctively. (a) LSVs of Ni_xFe_yOOH in KOH and SAW, (b) OER overpotentials at 10,100,200, 300 mA cm^{-2} for Ni_xFe_yOOH in KOH and SAW.

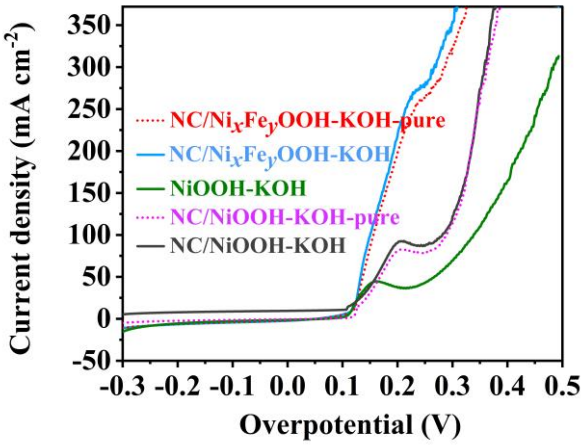

Figure S6. Influence of impurity iron in KOH electrolyte, sweeping from low to high potentials (positive sweep).

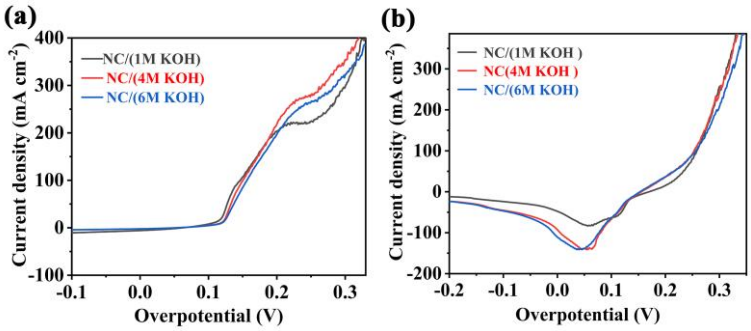

Figure S7. The activities of Ni_xFe_yOOH in different concentration of KOH with homogeneous distributed nickel clusters(NC). (a) The LSVs of NC/Ni_xFe_yOOH (positive sweep), (b) The LSVs of NC/Ni_xFe_yOOH (reversed sweep).

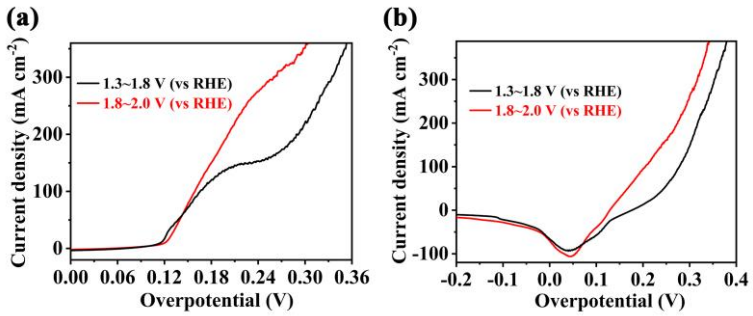

Figure S8. The effect of synthesizing nickel clusters (NC) with different cyclic voltammetry (CV) activation potentials on the activity of Ni_xFe_yOOH catalyst. (a) The LSVs of NC/Ni_xFe_yOOH (positive sweep), (b) The LSVs of NC/Ni_xFe_yOOH (reversed sweep).

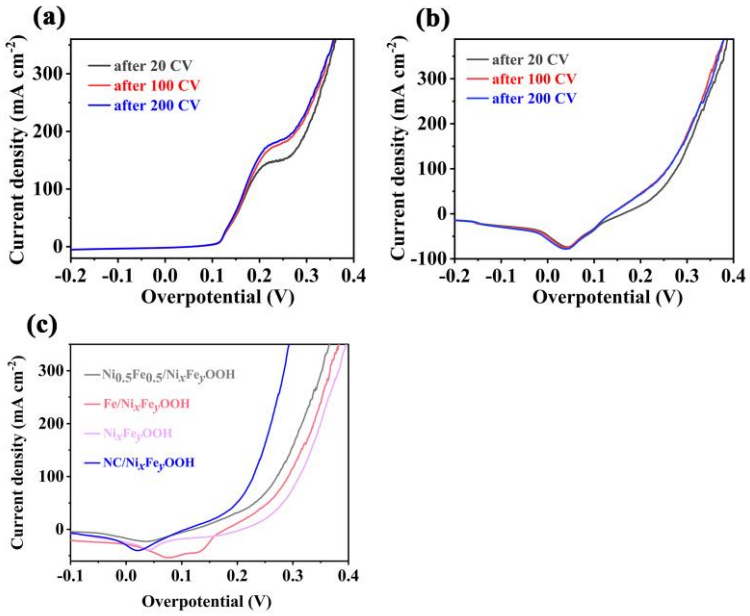

Figure S9. The effect of synthesizing nickel clusters (NC) with different cyclic voltammetry (CV) activation circles on the activity of Ni_xFe_yOOH catalyst. (a) The LSVs of NC/Ni_xFe_yOOH (positive sweep), (b) The LSVs of NC/Ni_xFe_yOOH (reversed sweep); (**c**) The polarization curves for NC/Ni_xFe_yOOH, $Ni_{0.5}Fe_{0.5}/Ni_xFe_yOOH$ and Fe/Ni_xFe_yOOH

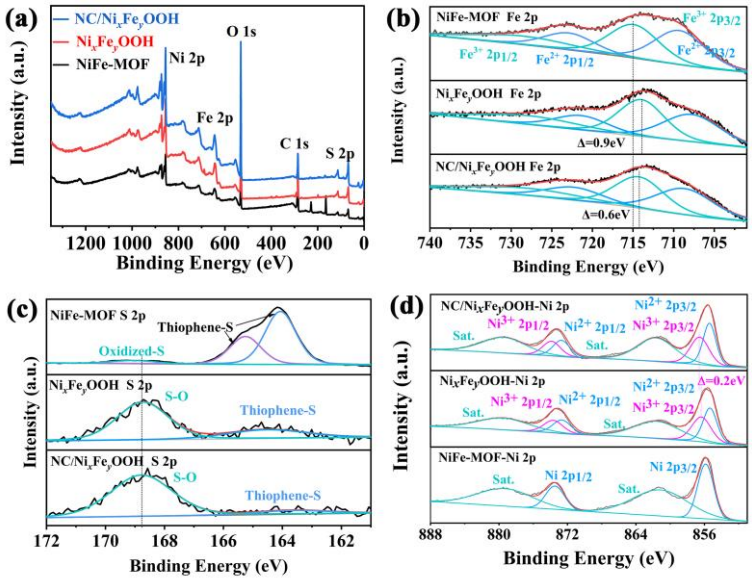

Figure S10. XPS spectra of NiFe-MOF, Ni_xFe_yOOH, and NC/Ni_xFe_yOOH.

(a) Survey scan of NiFe-MOF, High-resolution XPS spectra of (b) Fe 2p , (c) S 2p and (d) Ni 2p.

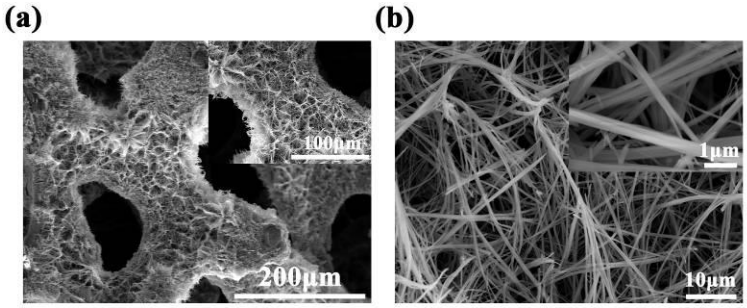

Figure S11. (a,b) SEM images of NC/Ni$_x$Fe$_y$OOH under different magnification the inset is partial enlarged detail.

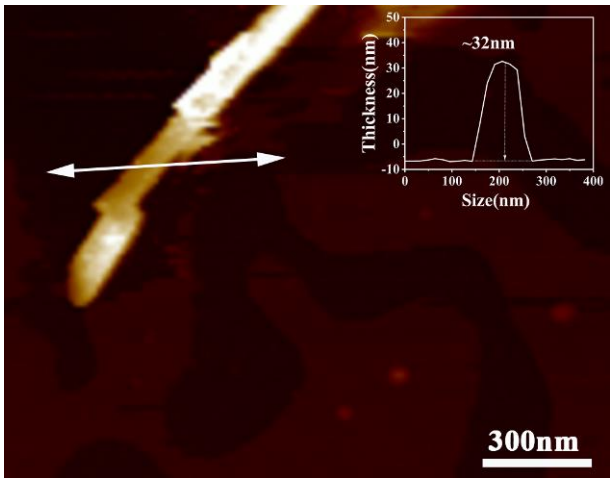

Figure S12. AFM image and corresponding height profile of NC/Ni$_x$Fe$_y$OOH.

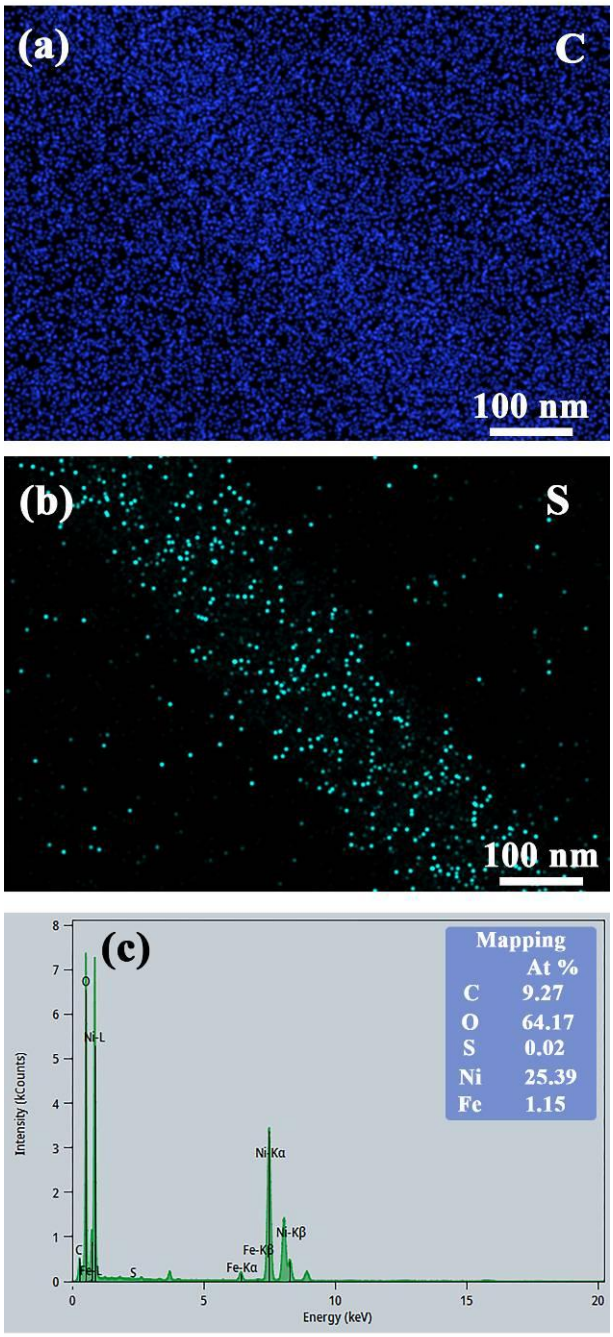

Figure S13. TEM Mappings of NC/Ni_xFe_yOOH.

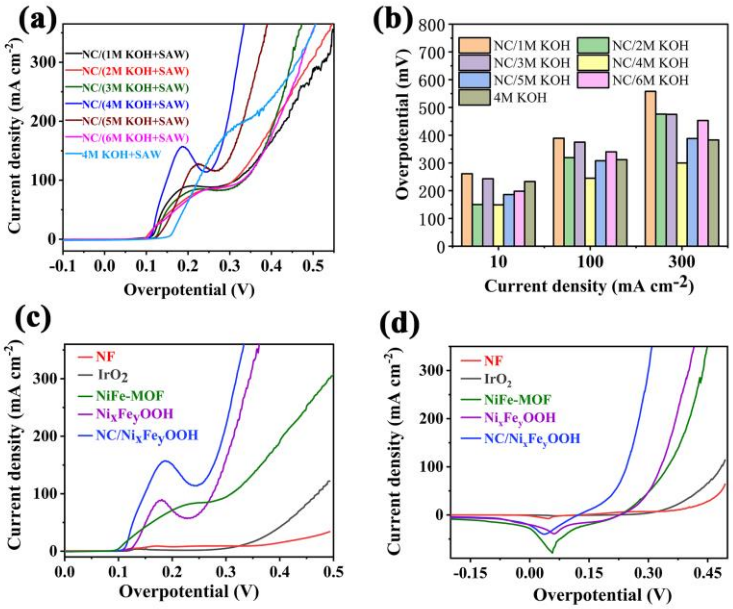

Figure S14. The activities of Ni_xFe_yOOH in NC/(1-6 M KOH+saline-alkali water (SAW)) mixed electrolyte. (a) LSVs (positive sweep) for NC/Ni_xFe_yOOH, (b) OER overpotentials at 10,100,300 mA cm^{-2} for NC/Ni_xFe_yOOH; (c) LSVs for NC/Ni_xFe_yOOH and its contrast samples (positive sweep), (d) LSVs for NC/Ni_xFe_yOOH and its contrast samples (reversed sweep).

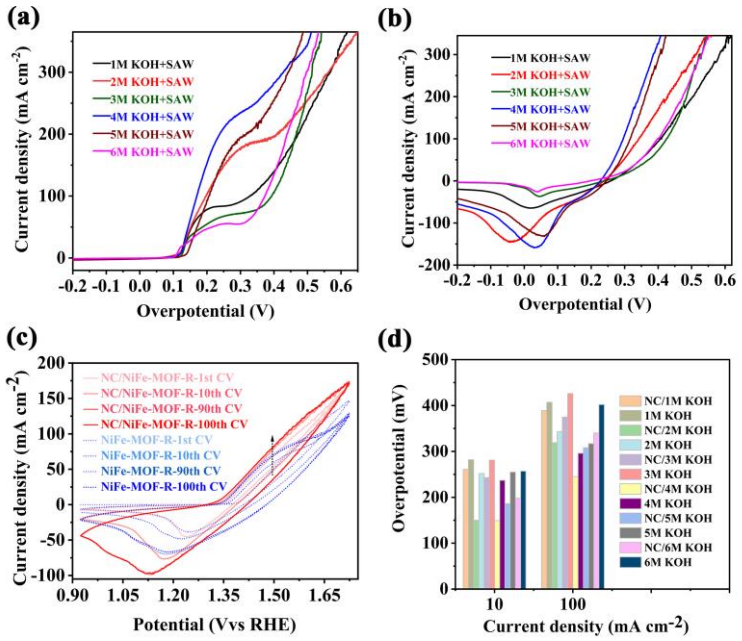

Figure S15.The activities of Ni_xFe_yOOH in 1-6 M KOH+saline-alkali water (SAW) mixed electrolyte. (a) LSVs (positive sweep) for Ni_xFe_yOOH, (b) LSVs (reversed sweep) for Ni_xFe_yOOH, (c) The activities of NiFe-MOF reconstitutions after different CV circles in 4 M KOH+saline-alkali water (SAW) and NC/ (4 M KOH+saline-alkali water (SAW))mixed electrolyte, respectively. (d) OER overpotentials at 10,100 mA cm^{-2} for Ni_xFe_yOOH and NC/Ni_xFe_yOOH, respectively.

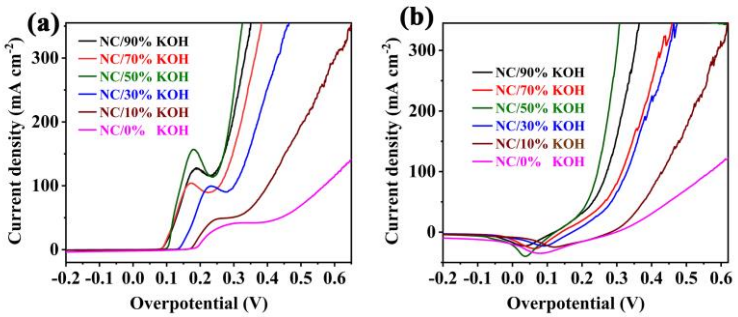

Figure S16. The activities of Ni_xFe_yOOH in NC/(4 M KOH+saline-alkali water (SAW)) mixed electrolyte with different volume fraction of KOH.

(a) The LSVs of NC/Ni_xFe_yOOH (positive sweep), (b) The LSVs of NC/Ni_xFe_yOOH(reversed sweep).

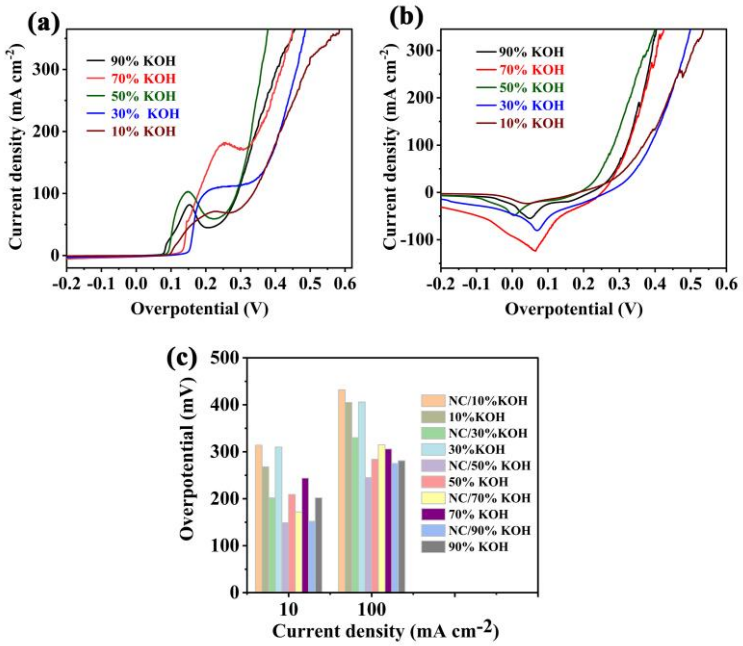

Figure S17. The activities of Ni_xFe_yOOH in 4 M KOH+saline-alkali water (SAW) mixed electrolyte with different volume fraction of KOH. (a) LSVs (positive sweep) for Ni_xFe_yOOH, (b) LSVs (reversed sweep) for Ni_xFe_yOOH, (c) OER overpotentials at 10,100 mA cm^{-2} for Ni_xFe_yOOH and NC/Ni_xFe_yOOH, respectively.

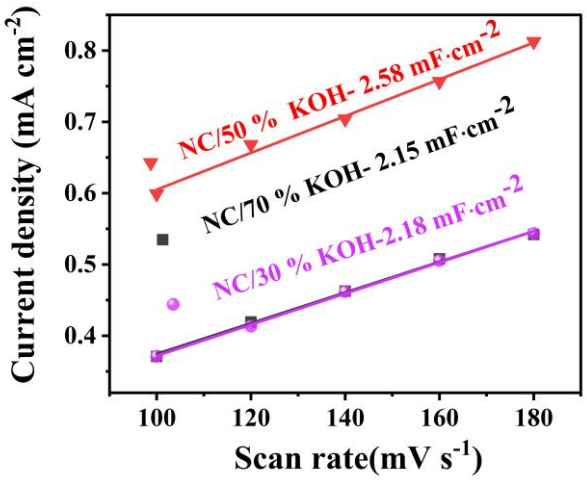

Figure S18. C_{dl} of Ni_xFe_yOOH in NC/(4 M KOH+saline-alkali water (SAW)) mixed electrolyte with different volume fraction of KOH.

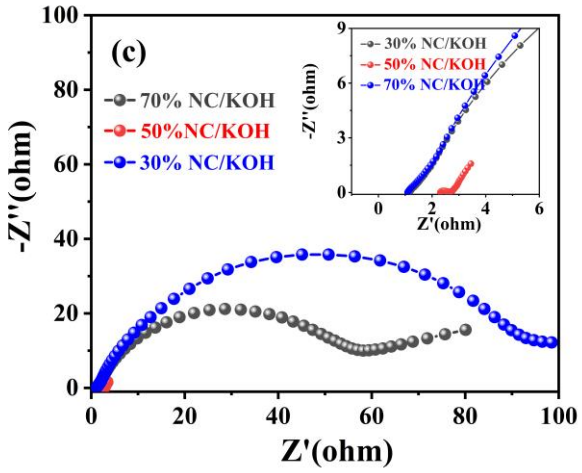

Figure S19. Nyquist plots of Ni_xFe_yOOH in NC/(4 M KOH+saline-alkali water (SAW)) mixed electrolyte with different volume fraction of KOH.

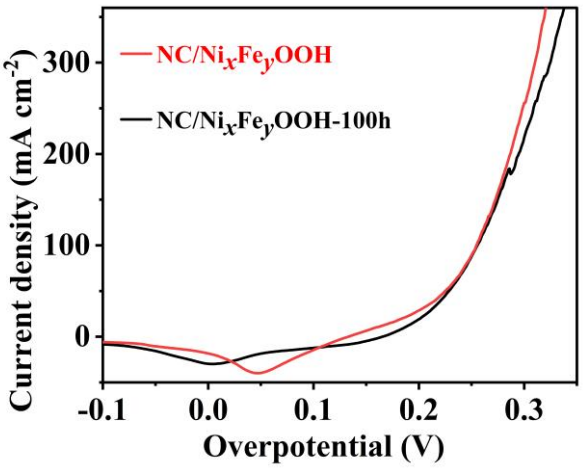

Figure S20. The activities of NC/Ni$_x$Fe$_y$OOH before and after 100 h chronopotentiometry measurement at 500 mA cm^{-2} without iR-compensation.

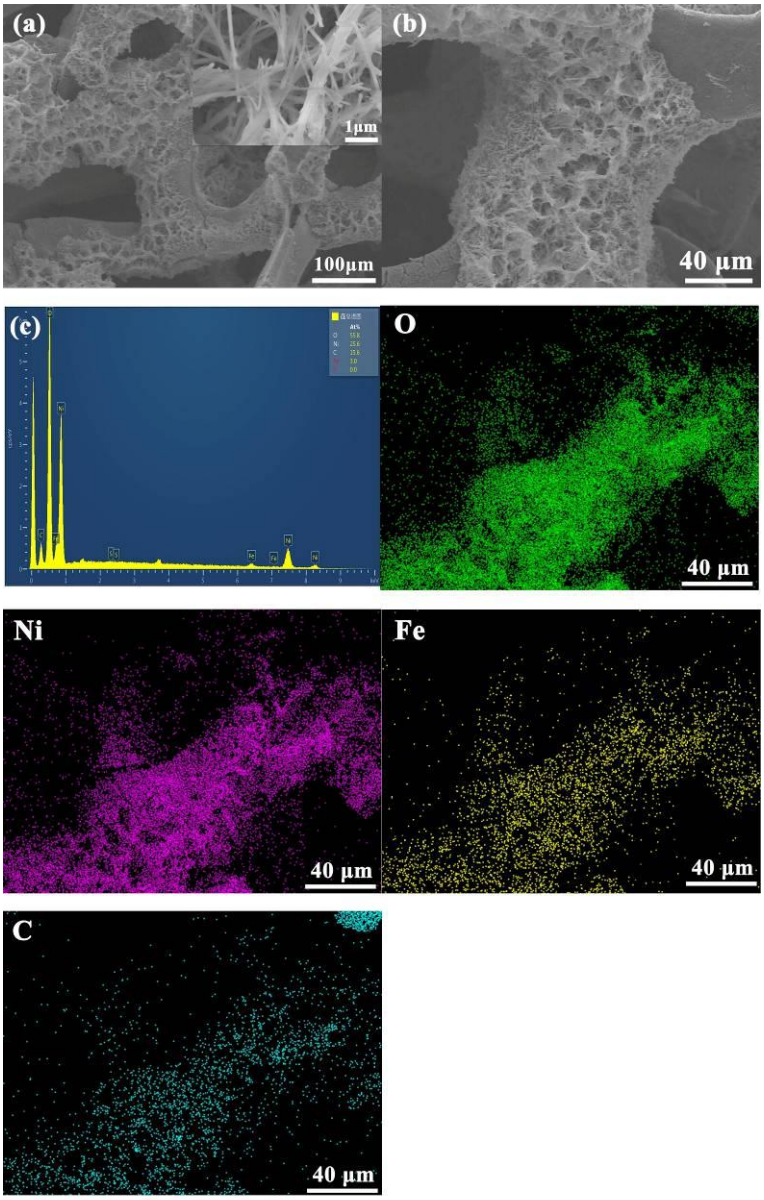

Figure S21. The structure of NC/Ni_xFe_yOOH before and after 100 h. chronopotentiometry measurement at 500 mA cm^{-2} without iR-compensation.

(a,b) SEM imges of NC/Ni_xFe_yOOH, (c) SEM Mapping of NC/Ni_xFe_yOOH.

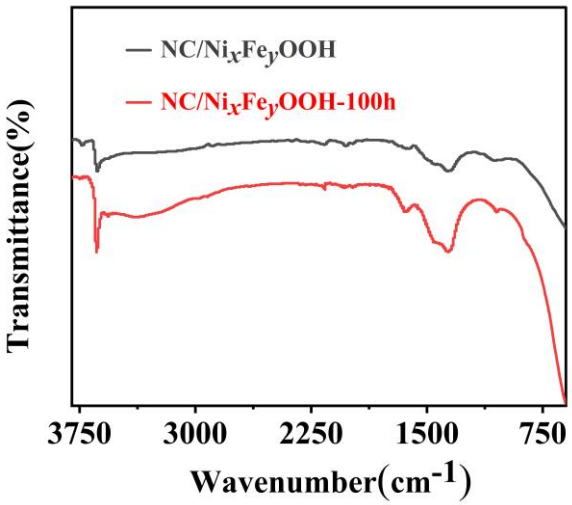

Figure S22. The FTIR spectra of NC/Ni$_x$Fe$_y$OOH before and after 100 h chronopotentiometry measurement at 500 mA cm^{-2} without iR-compensation.

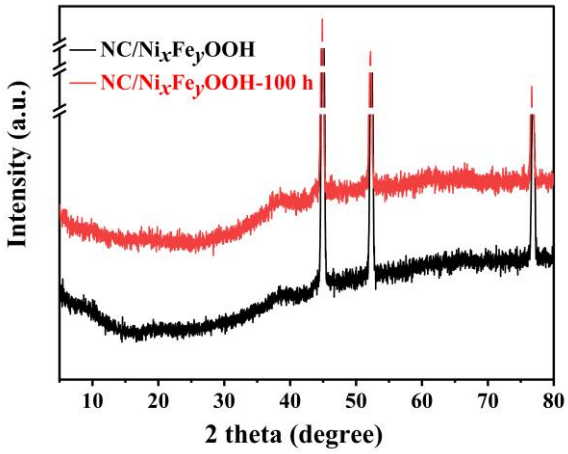

Figure S23. The XRD spectra of NC/Ni$_x$Fe$_y$OOH before and after 100 h chronopotentiometry measurement at 500 mA cm^{-2} without iR-compensation.

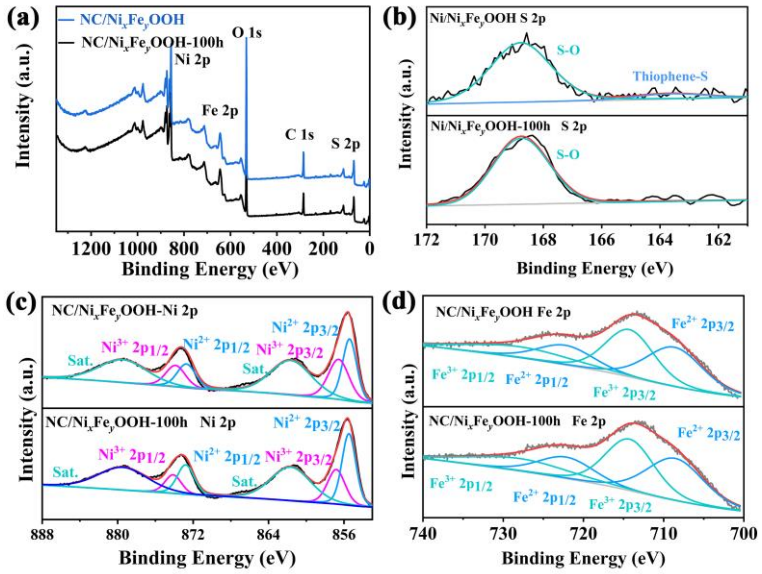

Figure S24. The XPS spectra of NC/Ni$_x$Fe$_y$OOH before and after 100 h chronopotentiometry measurement at 500 mA cm^{-2} without iR-compensation.

(a) Survey scan of NC/Ni$_x$Fe$_y$OOH and NC/Ni$_x$Fe$_y$OOH-100 h, High-resolution XPS spectra of (b) S 2p, (c) Ni 2p, and (d) Fe 2p.

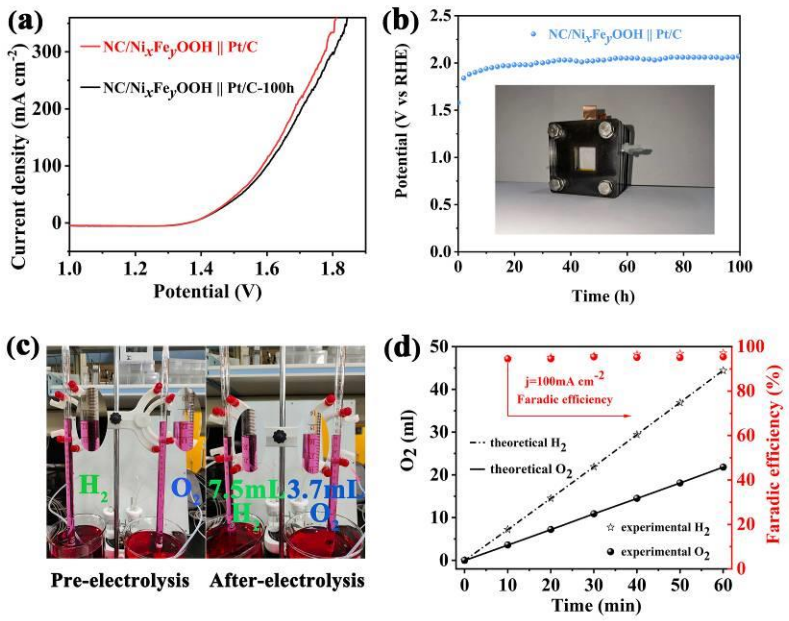

Figure S25. The overall water splitting performance of NC/Ni$_x$Fe$_y$OOH || Pt/C.

(a) The activities of NC/Ni$_x$Fe$_y$OOH before and after 100 h chronopotentiometry measurement at 500 mA cm^{-2} with 85% iR-compensation, (b) The chronopotentiometry curve of NC/Ni$_x$Fe$_y$OOH at 500 mA cm^{-2} for 100 h without-compensation, (c) Digital photograph of the equipment for measuring the volume of as-produced H_2/O_2 from overall water splitting, (d) FE in NC/(4 M KOH+SAW) (50 vol% KOH).

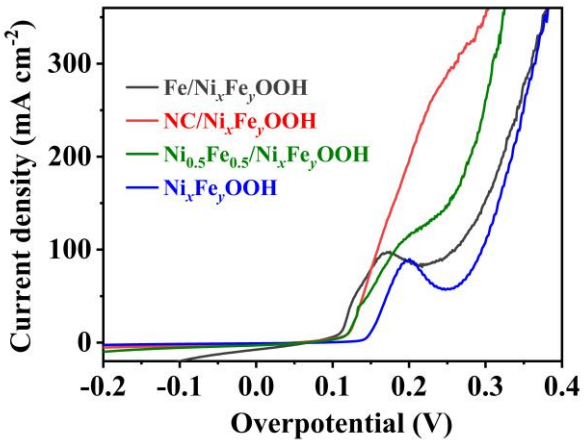

Figure S26. The effect of synthesizing different clusters (NC) on the activity of NC/Ni$_x$Fe$_y$OOH catalyst (positive sweep).

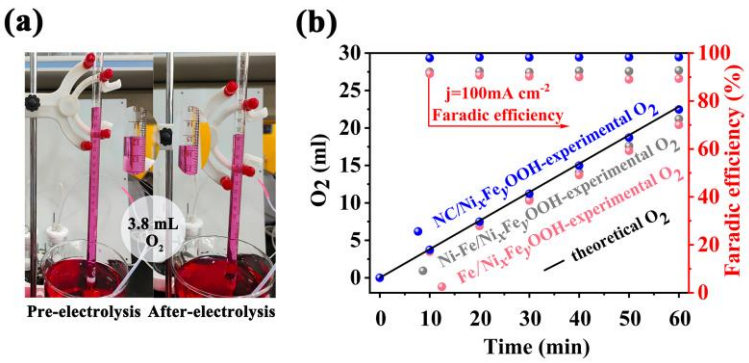

Figure S27. (a) Digital photograph of the equipment for measuring the volume of as-produced O_2, (b) FE operated in NC/(4 M KOH+SAW).

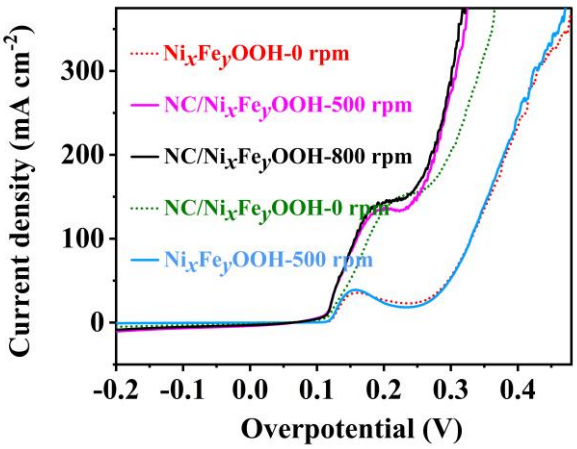

Figure S28. The effect of mechanical stirring rate on the activity of NC/Ni$_x$Fe$_y$OOH, and Ni$_x$Fe$_y$OOH.

Table S1a. ICP-MS analysis of saline-alkali water (SAW).

No.	Content (mg/L)			
	K	**Ca**	**Na**	**Mg**
1	1084	1766	1244	697

Table S1b. Component analysis of saline-alkali water (SAW).

No.	Content (mg/L)		
	HCO_3^-/CO_3^{2-}	**Cl^-**	**SO_4^{2-}**
1	151	1802	1146

Note: the component of HCO_3^-/CO_3^{2-} was measured by titration, the component of Cl^-, SO_4^{2-} was measured by ion chromatography method.

Table S2. ICP-MS analysis of nickel clusters (NC).

No.	Content (mg/L)
	Ni
1	**0.4**

Note: In order to eliminate the interference of impurities in KOH the electrolyte, the nickel clusters were prepared by CV activation of nickel foam in a high purity KOH electrolyte (99.999 wt%).

Table S3. Comparison of seawater OER activities with recently reported transition metal base electrocatalysts.

Catalysts	η_{10} (mV)	η_{100} (mV)	Electrolyte	Ref.
NC/Ni_xFe_yOOH	149	245	NC/(4 M KOH+SAW)	This work
BZ-NiFe-LDH/CC	/	300	1 M KOH+ seawater	4
Fe,P-$NiSe_2$ NFs	/	310	1 M KOH+ seawater	5
CoP_x@FeOOH	235	283	1 M KOH+ seawater	6
CoO@C/MXene/ NF	/	350	1 M KOH+ seawater	7
CoFe-NiOOH	200	266	6 M KOH+ seawater	8
Ni_2P-Fe_2P/NF	250	305	1 M KOH+ seawater	9
Ni_3S_2/Co_3S_4	280	360	1 M KOH+ seawater	10
NiCoFe-MOF	212	291	1 M KOH+ seawater	11
NiMoN@NiFeN	/	286	1 M KOH+ seawater	12
NiFe/NiS_x-Ni	/	370	1 M KOH+ seawater	13
S-(Ni,Fe)OOH	270	300	1 M KOH+ seawater	14
S,P-(Ni,Mo,Fe)OOH/Ni MoP/wood aerogel	/	286	1 M KOH+ seawater	15

Note: SAW: saline-alkali water, NC: nickel clusters.

Table S4. EIS simulation of NC/Ni_xFe_yOOH in 1-6 M NC/KOH+saline-alkali water (SAW) mixed electrolyte.

Model:

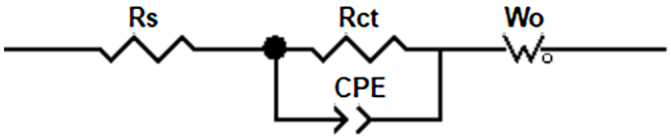

No.	Sample name	R_S/Ω	R_{ct}/Ω
1	NC/Ni_xFe_yOOH-1 M	0.68	44.75
2	NC/Ni_xFe_yOOH-2 M	0.83	17.89
3	NC/Ni_xFe_yOOH-3 M	1.21	0.78
4	NC/Ni_xFe_yOOH-4 M	0.81	0.29
5	NC/Ni_xFe_yOOH-5 M	1.27	9.13
6	NC/Ni_xFe_yOOH-6 M	1.04	14.57

Table S5. EIS simulation of NC/Ni_xFe_yOOH in 4 M NC/KOH+saline-alkali water (SAW) mixed electrolyte with different vol% KOH.

Model: 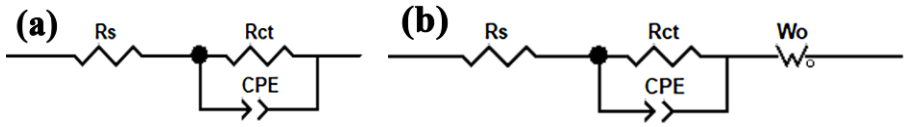

No.	Sample name	R_S/Ω	Rct/Ω	Model
1	NiFe-MOF-30%	1.09	48.03	b
2	NiFe-MOF-50%	0.81	0.29	b
3	NiFe-MOF-70%	1.14	104.5	a

Supporting References

1. McCrory, C. C.; Jung, S.; Peters, J. C.; Jaramillo, T. F., Benchmarking Heterogeneous Electrocatalysts for the Oxygen Evolution reaction. *J. Am. Chem. Soc.* **2013,** *135* (45), 16977-87.
2. Zheng, W.; Liu, M.; Lee, L. Y. S., Best Practices in Using Foam-Type Electrodes for Electrocatalytic Performance Benchmark. *ACS Energy Lett.* **2020,** *5* (10), 3260-3264.
3. Li, X.; Zhou, J.; Liu, C.; Xu, L.; Lu, C.; Yang, J.; Pang, H.; Hou, W., Encapsulation of Janus-structured Ni/Ni_2P Nanoparticles within Hierarchical Wrinkled N-doped Carbon Nanofibers: Interface Engineering Induces High-Efficiency Water Oxidation. *Appl. Catal. B-Environ* **2021,** *298*, 120578.
4. Zhang, L.; Liang, J.; Yue, L.; Dong, K.; Li, J.; Zhao, D.; Li, Z.; Sun, S.; Luo, Y.; Liu, Q.; Cui, G.; Ali Alshehri, A.; Guo, X.; Sun, X., Benzoate Anions-Intercalated NiFe-layered Double Hydroxide Nanosheet Array with Enhanced Stability for Electrochemical Seawater Oxidation. *Nano Research Energy* **2022,** *1*, e9120028.
5. Wu, L.; Yu, L.; Zhu, Q.; McElhenny, B.; Zhang, F.; Wu, C.; Xing, X.; Bao, J.; Chen, S.; Ren, Z., Boron-modified Cobalt Iron Layered Double Hydroxides for High Efficiency Seawater Oxidation. *Nano Energy* **2021,** *83*, 105838.
6. Wu, L.; Yu, L.; McElhenny, B.; Xing, X.; Luo, D.; Zhang, F.; Bao, J.; Chen, S.; Ren, Z., Rational Design of Core-shell-structured CoP @FeOOH for Efficient Seawater Electrolysis. *Appl. Catal. B-Environ* **2021,** *294*, 120256.
7. Zhang, L.; Wang, Z.; Qiu, J., Energy-Saving Hydrogen Production by Seawater Electrolysis Coupling Sulfion Degradation. *Adv. Mater.* **2022,** *34* (16), e2109321.
8. Huang, C.; Zhou, Q.; Yu, L.; Duan, D.; Cao, T.; Qiu, S.; Wang, Z.; Guo, J.; Xie, Y.; Li, L.; Yu, Y., Functional Bimetal Co-Modification for Boosting Large-Current-Density Seawater Electrolysis by Inhibiting Adsorption of Chloride Ions. *Adv. Energy Mater.* **2023,** *13* (32), 2301475.
9. Wu, L.; Yu, L.; Zhang, F.; McElhenny, B.; Luo, D.; Karim, A.; Chen, S.; Ren, Z., Heterogeneous Bimetallic Phosphide Ni_2P-Fe_2P as an Efficient Bifunctional Catalyst for Water/Seawater Splitting. *Adv. Funct. Mater.* **2020,** *31* (1), 2006484.
10. Wang, C.; Zhu, M.; Cao, Z.; Zhu, P.; Cao, Y.; Xu, X.; Xu, C.; Yin, Z., Heterogeneous Bimetallic Sulfides Based Seawater Electrolysis towards Stable Industrial-level Large Current Density. *Appl. Catal. B-Environ* **2021,** *291*, 120071.
11. Lan, C.; Xie, H.; Wu, Y.; Chen, B.; Liu, T., Nanoengineered, Mo-Doped, Ni_3S_2 Electrocatalyst with Increased Ni-S Coordination for Oxygen Evolution in Alkaline Seawater. *Energy & Fuels* **2022,** *36* (5), 2910-2917.
12. Yu, L.; Zhu, Q.; Song, S.; McElhenny, B.; Wang, D.; Wu, C.; Qin, Z.; Bao, J.; Yu, Y.; Chen, S.; Ren, Z., Non-noble Metal-nitride Based Electrocatalysts for High-performance Alkaline Seawater Electrolysis. *Nat. Commun.* **2019,** *10* (1), 5106.
13. Kuang, Y.; Kenney, M. J.; Meng, Y.; Hung, W. H.; Liu, Y.; Huang, J. E.; Prasanna, R.; Li, P.; Li, Y.; Wang, L.; Lin, M. C.; McGehee, M. D.; Sun, X.; Dai, H., Solar-driven, Highly Sustained Splitting of Seawater into Hydrogen and Oxygen Fuels. *PNAS* **2019,** *116* (14), 6624-6629.
14. Yu, L.; Wu, L.; McElhenny, B.; Song, S.; Luo, D.; Zhang, F.; Yu, Y.; Chen, S.; Ren, Z., Ultrafast Room-temperature Synthesis of Porous S-doped Ni/Fe (oxy)hydroxide Electrodes for Oxygen Evolution Catalysis in Seawater Splitting. *Energy Environ. Sci.* **2020,** *13* (10), 3439-3446.
15. Chen, H.; Zou, Y.; Li, J.; Zhang, K.; Xia, Y.; Hui, B.; Yang, D., Wood Aerogel-derived Sandwich-like Layered Nanoelectrodes for Alkaline Overall Seawater Electrosplitting. *Appl. Catal. B-Environ* **2021,** *293*, 120215.